Azimuthal Anisotropy and Lateral Heterogeneity Beneath Australia From Teleseismic P-wave Polarization Anomalies

K. Tarumi[1,2*] and K. Yoshizawa[1]

[1] Department of Earth & Planetary Sciences, Faculty of Science, Hokkaido University, Sapporo 060-0810, Japan.

[2] Earthquake Research Institute, The University of Tokyo, Tokyo, Tokyo 113-0032, Japan.

[*]Corresponding author: tarumi.kotaro.jp@gmail.com

This is a preprint that is submitted to EarthArXiv. The original manuscript has been submitted to Physics of the Earth and Planetary Interiors.

Azimuthal Anisotropy and Lateral Velocity Gradient Beneath Australia From Teleseismic P-wave Polarization Anomalies

Kotaro Tarumi[a,b,*,1], Kazunori Yoshizawa[a]

[a] *Department of Earth and Planetary Sciences, Faculty of Science, Hokkaido University, Sapporo, 060-0810, Japan*
[b] *Earthquake Research Institute, The University of Tokyo, Tokyo, Tokyo, 113-0032, Japan*

ARTICLE INFO

Keywords:
Azimuthal anisotropy
Lateral heterogeneity
P-waves
Polarization anomaly
Harmonic analysis
Bayesian inference

ABSTRACT

Teleseismic P-wave polarization anomalies provide useful constraints on lateral heterogeneity and anisotropic structure beneath seismic stations, but their application to continental-scale structures has remained limited. Here, we analyze long-period teleseismic P-wave polarization anomalies recorded at permanent and temporary seismic stations across Australia. We apply a harmonic analysis to the back-azimuth-dependent polarization anomalies to separate the contributions of the ϕ-term (lateral heterogeneity) and the 2ϕ-term (azimuthal anisotropy) using Bayesian inference. We then map the positive direction of the P-wave velocity gradient and the fast-axis direction, together with their uncertainties. The inferred directions of positive P-wave velocity gradients commonly correlate with crustal thinning along the continental margins, whereas several stations may reflect localized variations in the depth of the lithosphere-asthenosphere boundary (LAB). The spatial patterns of inferred fast-axis directions show clear tectonic-province-dependent variations. In eastern Phanerozoic Australia and the southern North Australian Craton, the anisotropy inferred from P-wave polarization anomalies is likely influenced by present-day asthenospheric mantle flow. In contrast, across much of cratonic Australia, the inferred fast-axis patterns are more plausibly attributed to frozen anisotropy within the lithosphere inherited from ancient tectonic processes. Our results demonstrate the potential of teleseismic P-wave polarization anomalies as a complementary dataset for investigating upper-mantle anisotropy beneath continents. Integrating these constraints with other seismological observations, such as receiver functions and surface-wave tomography, will help resolve the laterally variable and depth-dependent anisotropic architecture beneath the Australian continent and improve our understanding of its tectonic evolution.

1. Introduction

1.1. Seismic anisotropy and observational constraints

Seismic anisotropy is a key probe of the Earth's internal structure, past deformation, and present mantle dynamics, and is commonly described in terms of radial and azimuthal anisotropy. Radial anisotropy, representing the ratio between the horizontally-polarized SH and vertical-polarized SV wave speeds, is often related to the relative strength of mantle flow direction (e.g., Montagner and Tanimoto, 1991). Azimuthal anisotropy, which is the focus of this study, reflecting the direction-dependency of seismic-wave speed in the horizontal plane, has been investigated using a wide range of seismic datasets, including body-wave travel times (e.g., Liu and Zhao, 2016; Ishise et al., 2021), surface-wave (SW) dispersion (e.g., Tanimoto and Anderson, 1985; Montagner and Tanimoto, 1990; Debayle et al., 2005), PKS/SKS

*Corresponding author
tarumi.kotaro.jp@gmail.com (K. Tarumi)
ORCID(s): 0009-0002-9030-5408 (K. Tarumi); 0000-0003-2282-3748 (K. Yoshizawa)

(XKS) splitting analyses (e.g., Vinnik et al., 1992; Heintz and Kennett, 2005; Wolf et al., 2025), and teleseismic P-wave polarization anomalies (e.g., Schulte-Pelkum et al., 2001; Cristiano et al., 2016).

SW tomography has been widely used to estimate large-scale azimuthally anisotropic structure in the upper mantle, with good vertical sensitivity (e.g., Debayle et al., 2005; de Laat et al., 2023). However, because of their long wavelengths, SW data are less sensitive to rapid lateral variations than body-wave observables (Maupin and Park, 2015). In contrast, body-wave data, such as XKS splitting and P-to-SH conversions, can resolve anisotropic properties beneath the vicinity of seismic stations, and are therefore effective for mapping lateral variations when dense seismic arrays are available (e.g., Eakin et al., 2021), although their depth-integrated characters limit the vertical resolution (e.g., Maupin and Park, 2015). Combining these complementary datasets is therefore important for resolving crust-mantle anisotropy and improving our understanding of past deformation and present mantle dynamics (e.g., Wüstefeld et al., 2009; Yuan and Romanowicz, 2010).

XKS splitting analyses have been widely used to investigate azimuthal anisotropy using body-wave data (e.g., Wüstefeld et al., 2009; Wolf et al., 2025). Teleseismic P-wave polarization anomalies provide another useful constraint on localized anisotropic structure near the receiver (Crampin et al., 1982; Schulte-Pelkum et al., 2001; Schulte-Pelkum and Blackman, 2003). Ideally, teleseismic P-waves arrive from the source direction and oscillate in the vertical-radial plane. However, in the real Earth, P-waves can exhibit anomalous polarization because of lateral heterogeneity (e.g., Frederiksen and Bostock, 2000) and azimuthal anisotropy (Crampin et al., 1982) in the vicinity of the receiver (Figure S1).

Schulte-Pelkum et al. (2001) modeled teleseismic P-wave polarization anomalies using a harmonic expansion with 1ϕ and 2ϕ dependencies, where ϕ denotes the back-azimuth, and estimated both station misorientations and anisotropic properties associated with the 2ϕ term. They also showed that this observable can be sensitive to seismic structures to depths of ~250 km, despite limited vertical resolution (Schulte-Pelkum et al., 2001). The fast-axis directions inferred from P-wave polarization anomalies were generally consistent with those inferred from XKS splitting analyses, suggesting sensitivity to upper-mantle anisotropy (Schulte-Pelkum et al., 2001). At the same time, interpretation requires caution because the 1ϕ term can include contributions from lateral heterogeneity (Schulte-Pelkum and Blackman, 2003). Fontaine et al. (2009) and Cristiano et al. (2016) further showed that the positive direction of P-wave velocity gradient inferred from the 1ϕ dependency can correlate with crustal and/or uppermost mantle structure in Australia and southern Germany, respectively. These studies suggest that harmonic analysis of teleseismic P-wave polarization anomalies provides complementary constraints on anisotropic structure and lateral velocity variations in the crust and upper mantle.

1.2. Heterogeneous and anisotropic structure of the Australian continent

The Australian continent was assembled during the mid-Proterozoic through the cratonic amalgamation of three major cratonic blocks in western and central Australia (1600–1000 Ma; Myers et al., 1996), the West Australian Craton (WAC), North Australian Craton (NAC), and South Australian Craton (SAC) (Figure 1 (a)). The WAC mainly comprises the Archean Pilbara and Yilgarn cratons, whereas the NAC and SAC were largely formed during the Proterozoic. Between these cratonic provinces lies a suture zone that likely acted as a buffer during ancient cratonic collisions (Yoshida, 2012; Yoshida and Yoshizawa, 2020), recording deformation associated with cratonic amalgamation. In contrast, eastern Australia is a Phanerozoic orogenic domain formed through back-arc spreading related to Tonga–Kermadec subduction (e.g., Glen, 2005). The Australian continent separated from Antarctica at ∼100 Ma (e.g., Veevers, 2004) and is now one of the fastest-moving continental plates, drifting northward at 6–7 cm/yr (e.g., Argus et al., 2011). This tectonic diversity makes Australia an ideal region for investigating cratonic evolution and complex seismic structures, including anisotropy.

Seismological studies across Australia have revealed large-scale lateral heterogeneity and anisotropy of S-waves (e.g., Debayle and Kennett, 2000; Yoshizawa and Kennett, 2004; Fishwick et al., 2008; Yoshizawa, 2014; de Laat et al., 2023) as well as major seismic discontinuities (e.g., the Moho and Lithosphere–Asthenosphere Boundary; LAB) (e.g., Ford et al., 2010; Yoshizawa, 2014; Birkey et al., 2021; Birkey and Ford, 2023; de Laat et al., 2023; Tarumi and Yoshizawa, 2025a). The Moho generally deepens from the continental margin toward central Australia and exhibits complex topography near the suture zone, with depth variations that do not simply correlate with geological age (Kennett et al., 2023). In contrast, lithospheric thickness varies among tectonic provinces (e.g., Kennett et al., 2013; Yoshizawa, 2014; Yoshizawa and Kennett, 2015; Magrini et al., 2023). Eastern Phanerozoic Australia is characterized by a relatively shallow LAB (typically 60–100 km; e.g., Kennett et al., 2013), with localized rapid variations near tectonic boundaries such as the Tasman Line (Figure 1 (a) Fishwick et al., 2008; Tarumi and Yoshizawa, 2025a). Beneath the cratonic blocks and the suture zone, the lithosphere is significantly thicker (120–220 km) and becomes thinner toward the continental margins (Kennett et al., 2013; Yoshizawa, 2014; Magrini et al., 2023).

Azimuthal anisotropy beneath Australia has been extensively investigated using SW tomography (e.g., Debayle and Kennett, 2000; Debayle et al., 2005; Fishwick et al., 2008; Debayle et al., 2016; de Laat et al., 2023), XKS splitting analyses (e.g., Özalaybey and Chen, 1999; Heintz and Kennett, 2005; Bello et al., 2019; Chen et al., 2021a; Ba et al., 2023; Eakin et al., 2021, 2023), and azimuth-dependent P-wave receiver functions (Chen et al., 2021b; Birkey and Ford, 2023). These studies reveal complex anisotropic architectures in the upper mantle that vary among the cratonic blocks, the suture zone, and eastern Phanerozoic Australia (Ba et al., 2023; de Laat et al., 2023; Birkey and Ford, 2023). In regions with thinner lithosphere, fast-axis directions are generally consistent with plate motion, suggesting a dominant contribution from asthenospheric mantle flow, particularly in southeastern Australia (Eakin et al., 2023;

Ba et al., 2023; Fishwick et al., 2008; de Laat et al., 2023). In contrast, cratonic regions commonly exhibit anisotropic patterns interpreted as frozen anisotropy preserved in the thick lithosphere, likely reflecting ancient tectonic processes (Chen et al., 2021b; Eakin et al., 2021; de Laat et al., 2023; Gauntlett et al., 2025). However, regional discrepancies remain between XKS splitting results and large-scale SW tomographic models (e.g., Eakin et al., 2023; Gauntlett et al., 2025), and the detailed anisotropic structure beneath Australia is still debated.

1.3. Scope of this study

Applications of teleseismic P-wave polarization anomalies to the study of azimuthal anisotropy beneath Australia at the continental scale have yet to be explored. Previous studies of this kind have included a small number of Australian stations as part of broader analyses Schulte-Pelkum et al. (2001); Fontaine et al. (2009). In addition, many regional P-wave travel-time tomography studies have focused on isotropic velocity structures and have not explicitly incorporated anisotropic effects (e.g., Rawlinson et al., 2014; Davies et al., 2015; Sun and Kennett, 2016). Therefore, anisotropic properties based on P waves at the continental scale remain poorly constrained.

In this study, we employ teleseismic P-wave polarization anomaly data measured at permanent and temporary stations across Australia to map, at the continental scale, both (1) lateral heterogeneity represented by the P-wave velocity-gradient direction and (2) fast-axis orientations associated with anisotropic fabrics. We then explore possible causes of the inferred P-wave velocity-gradient directions by comparing them with Moho and LAB topography. We also compare the inferred anisotropy distribution with previous XKS splitting analyses (e.g., Eakin et al., 2021; Ba et al., 2023) and SW tomography models (e.g., de Laat et al., 2023), and discuss their origins in the context of Australian tectonic evolution.

In addition, we aim to provide an independent observational constraint using teleseismic P-wave polarization anomaly data. Because teleseismic P-wave polarization anomalies have limited vertical resolution, the inferred parameters are best interpreted as path-integrated constraints rather than depth-localized estimates. Since this observable has different sensitivities and sampling geometry compared with XKS splitting and SW data (Figure S2), this approach provides an independent perspective on anisotropic structure beneath Australia, and complements existing interpretations.

2. Data: Teleseismic P-wave polarization anomaly

Our dataset comprises long-period teleseismic P-wave polarization anomalies obtained by Tarumi and Yoshizawa (2025c), which provide dense spatial coverage across Australia. In our previous study, we measured the arrival angles of long-period teleseismic P-waves recorded at permanent and temporary seismic stations in and around Australia. The polarization anomaly, defined as the deviation of the arrival angle from the station orientation (Tarumi and

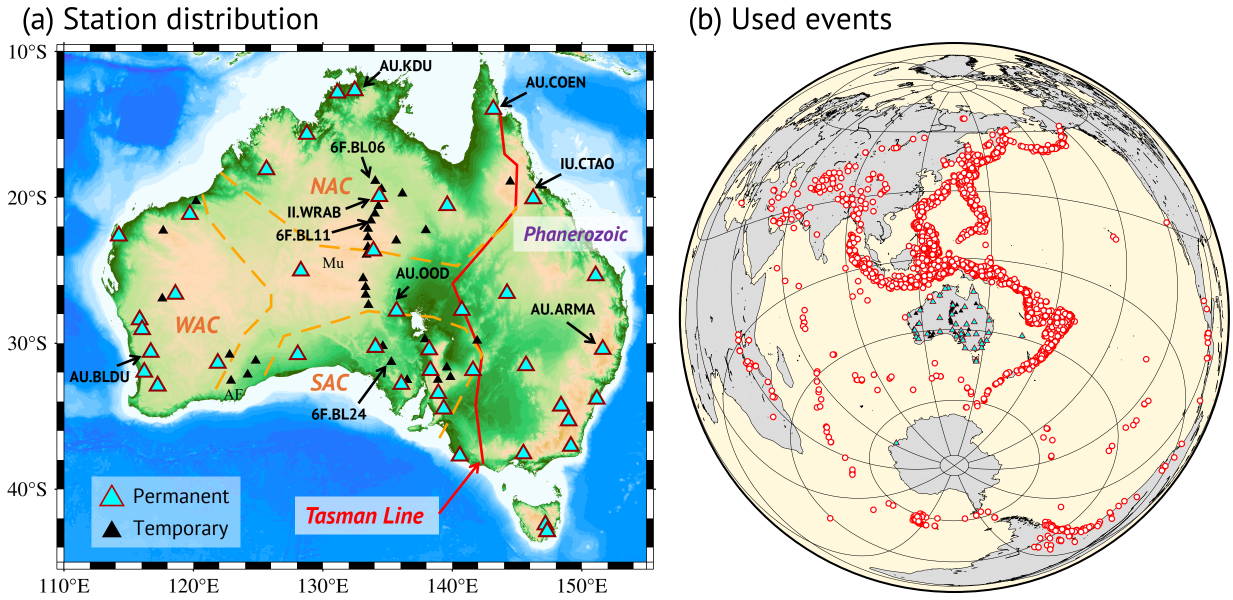

Figure 1: Map view of station distribution and seismic events used in this study. (a) Station distribution across Australia. Cyan and black triangles represent permanent and temporary stations, respectively. Orange dashed lines indicate major cratonic boundaries in Australia (WAC: West Australian Craton; NAC: North Australian Craton; SAC: South Australian Craton). The red line marks the Tasman Line, the geological boundary between Phanerozoic and cratonic Australia. Selected stations are labeled with station names and black arrows; examples are shown in Figures 2 and 5. "AF" and "Mu" represent Albany-Fraser Orogeny and Musgrave Province, respectively. (b) Event distribution used to measure the P-wave polarization anomaly. White dots with red circles indicate seismic events used in this study. Cyan and black triangles are the same as in (a).

Yoshizawa, 2025c), clearly depends on the back-azimuth angle (Tarumi and Yoshizawa, 2025c). Here, we analyze the back-azimuthal variations in the polarization angle at these stations. Prior to the processing described below, we discarded stations with fewer than 30 arrival-angle measurements because the back-azimuthal patterns could not be sufficiently resolved. The resulting station and seismic event distributions used in this study are shown in Figure 1.

We first subtracted the station orientation estimated in Tarumi and Yoshizawa (2025c) from the measured arrival angles to set a common reference in which 0° corresponds to the corrected station orientation. We then computed the median polarization angle within each 20° back-azimuth bin. For each bin, we also calculated the standard error of the polarization angles and the median back-azimuth, which are used as weights in the inversion described in the next section. Figures 2 and 3 show the number of data in the 20° back-azimuth bin and the clockwise polarization anomaly from the station orientation at seven permanent and three temporary stations.

The events used in this study are concentrated to the northwest, north, and east of Australia (Figure 1). The azimuthal coverage varies with the station location, leading to station-dependent uncertainty in the polarization anomaly data (Figures 2 and 3). At all stations, the standard errors, treated as the data uncertainties in this study, tend to be larger for back-azimuths from the southeast to the west ($140 < \phi < 280$) than for other back-azimuths. To mitigate bias arising from the uneven event distribution, we introduce Bayesian inference into the harmonic analysis

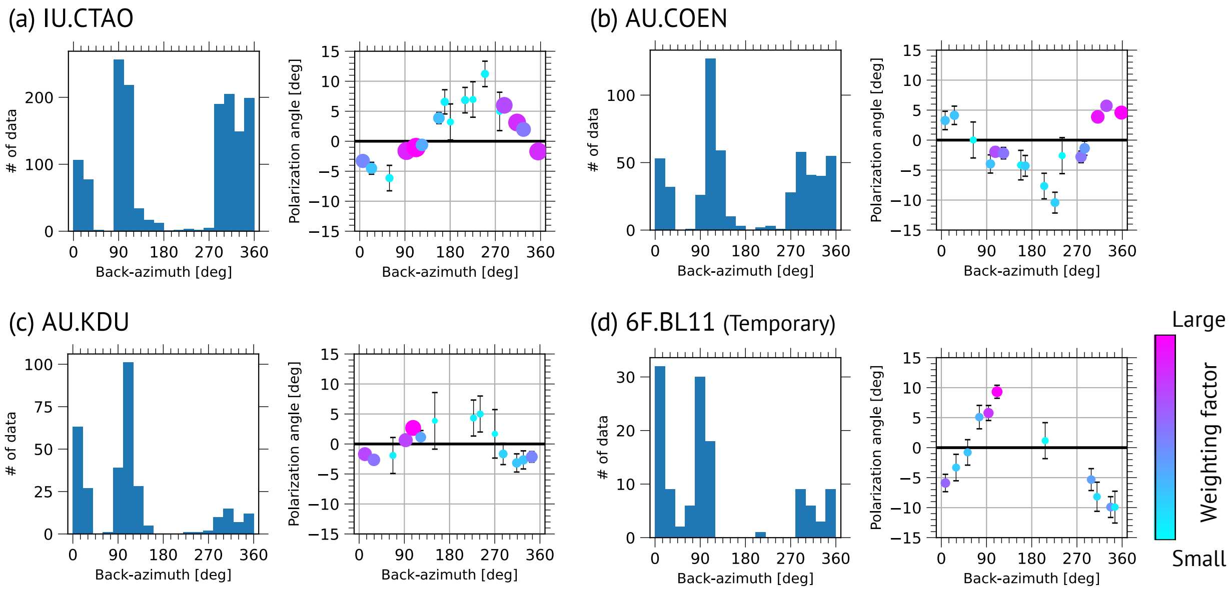

Figure 2: Examples of P-wave polarization anomaly data at three permanent stations (a: IU.CTAO; b: AU.COEN; c: AU.KDU) and one temporary station (d: 6F.BL11). For each station, the left panel shows a histogram of the number of events. The right panel shows the polarization anomaly data after the binning procedure described in the main text. Error bars represent the binned standard error. The colors of the dots reflect the relative magnitude of the standard error, which is used for the harmonic analyses in the Method section.

of the polarization anomaly data. For the temporary stations, the number of measurements is much smaller than at the long-running permanent stations (Figures 2 (d) and 3 (e, f)).

Figure 2 shows the polarization anomaly data at IU.CTAO, AU.COEN, AU.KDU, and 6F.BL11, which exhibit relatively strong 360° periodicity with back-azimuth ϕ. In particular, the polarization anomaly at IU.CTAO (Figure 2-(a)) is very close to that reported by Fontaine et al. (2009), illustrating a sinusoidal trend. This pattern suggests that lateral velocity gradients can significantly deflect the apparent incoming direction of teleseismic P-waves (Schulte-Pelkum et al., 2001; Fontaine et al., 2009). The other three stations likely also reflect lateral heterogeneity in the vicinity of the stations.

On the other hand, in Figure 3, we observe clear back-azimuthal dependencies with near 180° periodicity, instead of 360° periodicity. Particularly, the polarization data at II.WRAB and AU.BLDU (Figure 3-(a) and (c)) show clear 180° periodicity, which is attributed to azimuthal anisotropy beneath the station, reflecting anisotropy in the horizontal plane. In this study, we estimate the fast-propagating direction of teleseismic P-waves from these polarization anomaly data.

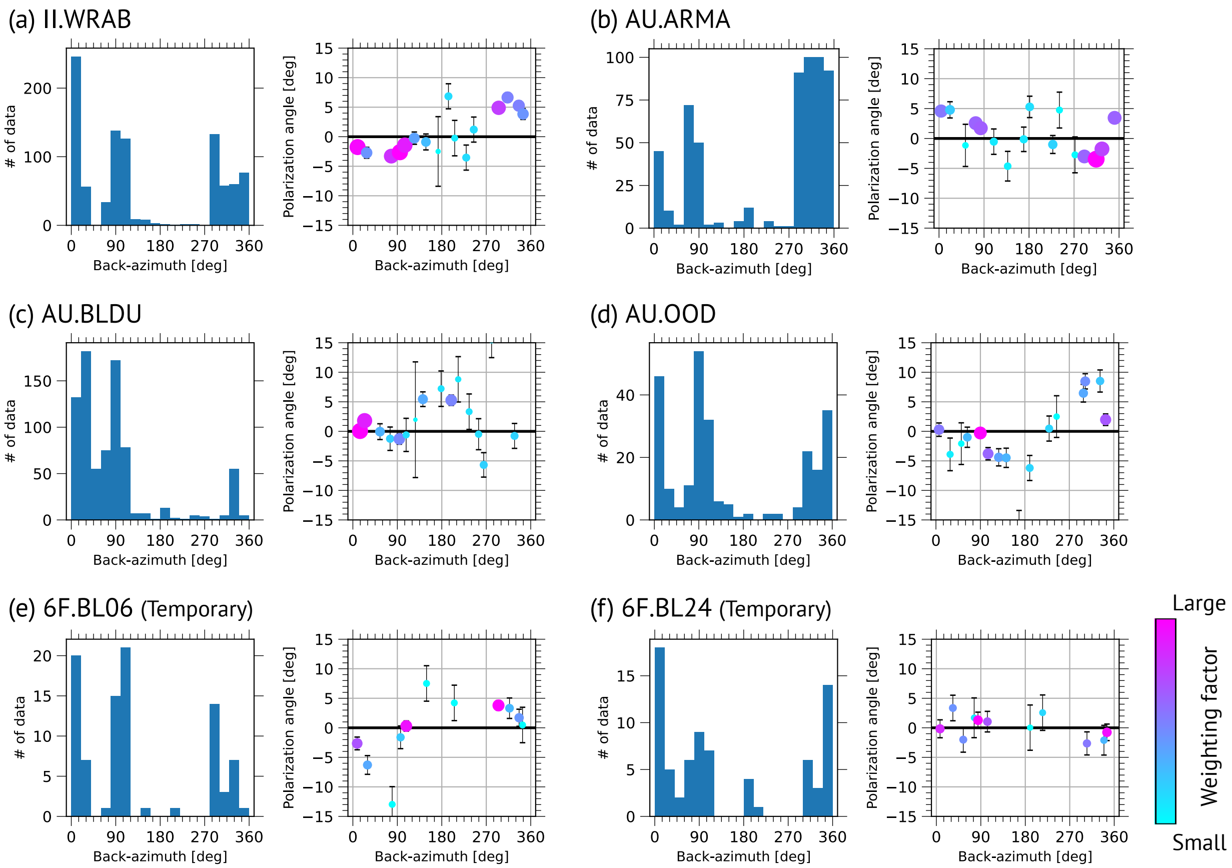

Figure 3: Same as Figure 2, but for other six stations (a: II.WRAB; b: AU.ARMA; c: AU.BLDU; d: AU.OOD; e: 6F.BL06; f: 6F.BL24). (a–d) Permanent stations. (e, f) Temporary stations.

3. Method

We applied harmonic analysis to the binned, statistically processed P-wave polarization anomaly data, following previous studies (Schulte-Pelkum et al., 2001; Fontaine et al., 2009; Cristiano et al., 2016), to explain the observed back-azimuthal trend. The harmonic expansion is defined as,

$$\delta\eta(\phi) = A_0 + A_1 \sin\phi + A_2 \cos\phi + A_3 \sin 2\phi + A_4 \cos 2\phi, \tag{1}$$

where $\delta\eta(\phi)$ is the anomaly of arrival angle as a function of back-azimuth ϕ, and $A_{i=1,\ldots,4}$ are coefficients of the sinusoidal terms (Schulte-Pelkum et al., 2001). The constant term A_0 corresponds to station misorientation, which shifts the arrival angle independently of back-azimuth. Because we have already estimated the time-dependent misorientation for each station (Tarumi and Yoshizawa, 2025c), Equation (1) is reformulated as

$$\delta\eta(\phi) - A_0 = A_1 \sin\phi + A_2 \cos\phi + A_3 \sin 2\phi + A_4 \cos 2\phi, \tag{2}$$

where the left-hand side represents the polarization anomaly defined in this study. The coefficient pair (A_1, A_2) and (A_3, A_4) primarily reflect lateral heterogeneity in seismic structure (e.g., the dipping interfaces) and azimuthal anisotropy beneath and around seismic station, respectively, and are treated as model parameters in this study.

We express the direction of positive seismic velocity gradient (i.e., the direction in which seismic wave speed increases) at depth as

$$\theta_{\mathrm{hetero}} = \mathrm{atan2}(A_1, A_2) + 90^\circ. \tag{3}$$

Here, $\mathrm{atan2}(y, x)$ denotes the four-quadrant inverse tangent function that accounts for the signs of both x and y and returns an angle in the range $(-\pi, \pi]$. The fast-axis direction of azimuthal anisotropy is associated with the 180° periodicity in the data and is derived following (Fontaine et al., 2009; Cristiano et al., 2016):

$$\theta_{\mathrm{fast}} = \frac{1}{2}\mathrm{atan2}(A_3, A_4) + 45^\circ. \tag{4}$$

Both θ_{hetero} and θ_{fast} can be interpreted as representing path-integrated directions.

After estimating $A_{i=1,\ldots,4}$, we quantify whether the heterogeneity or anisotropy term better explain the observed data, $\delta\eta(\phi)$. Following Fontaine et al. (2009), we introduce the magnitude ratio between the ϕ-term and 2ϕ-term,

$$\Delta = \frac{\sqrt{A_3^2 + A_4^2}}{\sqrt{A_1^2 + A_2^2}} = \frac{A_{\mathrm{fast}}}{A_{\mathrm{hetero}}}. \tag{5}$$

If $\Delta \ll 1$, lateral heterogeneity significantly influences the arrival angle of teleseismic P-waves, and vice versa.

For solving the harmonic equation (2), we employed hierarchical Bayesian inference to estimate the posterior probability density functions of $\mathbf{m} = (A_1, A_2, A_3, A_4)$ and σ:

$$p(\mathbf{m}|\delta\eta(\phi)) \propto p(\delta\eta(\phi)|\mathbf{m}, \sigma)p(\mathbf{m})p(\sigma), \tag{6}$$

where $p(x)$ represents the probability density of x. The right-hand side of Equation (6) represents the posterior distribution to be inferred. $p(\delta\eta(\phi)|\mathbf{m}, \sigma)$ denotes the likelihood function, which is assumed to follow a normal distribution:

$$p(\delta\eta(\phi)|\mathbf{m}, \sigma) = \frac{1}{\sigma\sqrt{2\pi}} \exp\left(-\frac{\|\Phi(\mathbf{m}, \delta\eta(\phi))\|^2}{2\sigma^2}\right), \tag{7}$$

where $\Phi(\mathbf{m}, \delta\eta(\phi))$ is a weighted misfit function and σ represents the overall uncertainty of the polarization anomaly data. Because the event distribution around Australia is uneven, with many events located in Indonesia, Japan, and the Tonga-Kermadec trench, we define the weighted misfit function by accounting for bin-dependent measurement uncertainty:

$$\Phi(\mathbf{m}, \delta\eta(\phi)) = (\delta\eta(\phi) - \mathbf{g}(\mathbf{m})) \cdot \frac{\sqrt{N_{bin}}}{\sigma_{bin}}, \tag{8}$$

where σ_{bin} and N_{bin} are the standard deviation and the number of measurements of polarization angles in each 20° bin, respectively; the misfit function is therefore weighted by the inverse of standard errors in each bin. Finally, $p(\mathbf{m})$ and $p(\sigma)$ denote the prior distributions of $\mathbf{m}$ and σ, which are assumed to be uniform over $[-25, 25]$ and $[0, 20]$, respectively.

To perform the inference, we used PyMC (Abril-Pla et al., 2023), a probabilistic programming framework for Bayesian modeling. We then transformed the posterior samples of (A_1, A_2, A_3, A_4) into the posterior distributions of the ϕ-term and 2ϕ-term (A_{hetero} and A_{fast}; θ_{hetero} and θ_{fast}). From these posterior distributions, we computed representative parameters; including the mean, circular mean, mode, and the first and third quartiles. Because the resulting distributions do not always follow a normal distribution, we adopted the interquartile range (IQR) as a measure of uncertainty for θ_{hetero} and θ_{fast}, corresponding to the central 50 % credible interval. In subsequent sections, we discarded stations with IQR> 40°.

4. Result

4.1. Individual Bayesian inversion results

Figures 4 and 5 show the results of the Bayesian inference for the polarization anomaly data at the six stations shown in Figures 2 and 3. In each figure, the leftmost panels show the objective binned anomaly data, the predicted ensemble solutions, and the mean solution. The posterior predictions reproduce the binned anomaly data well, demonstrating that the inverted models adequately fit the objective data. The other panels show the posterior histograms of A_{hetero}, θ_{hetero}, A_{fast}, and θ_{fast}, respectively. The magnitudes of A_{hetero} and A_{fast} reflect the relative contributions of lateral heterogeneity and azimuthal anisotropy to the observed P-wave polarization anomalies, respectively. The angles of θ_{hetero} and θ_{fast} represent the directions in which teleseismic P-wave propagate faster; θ_{hetero} corresponds to the direction of the positive P-wave velocity gradient, whereas θ_{fast} represents the fast-axis direction of P-wave azimuthal anisotropy at depth.

Figure 4 shows the Bayesian inversion results for (a) IU.CTAO, (b) AU.COEN, and (c) 6F.BL11. For all three stations, the inverted model reproduces the observed polarization anomaly data and captures the pronounced 360°

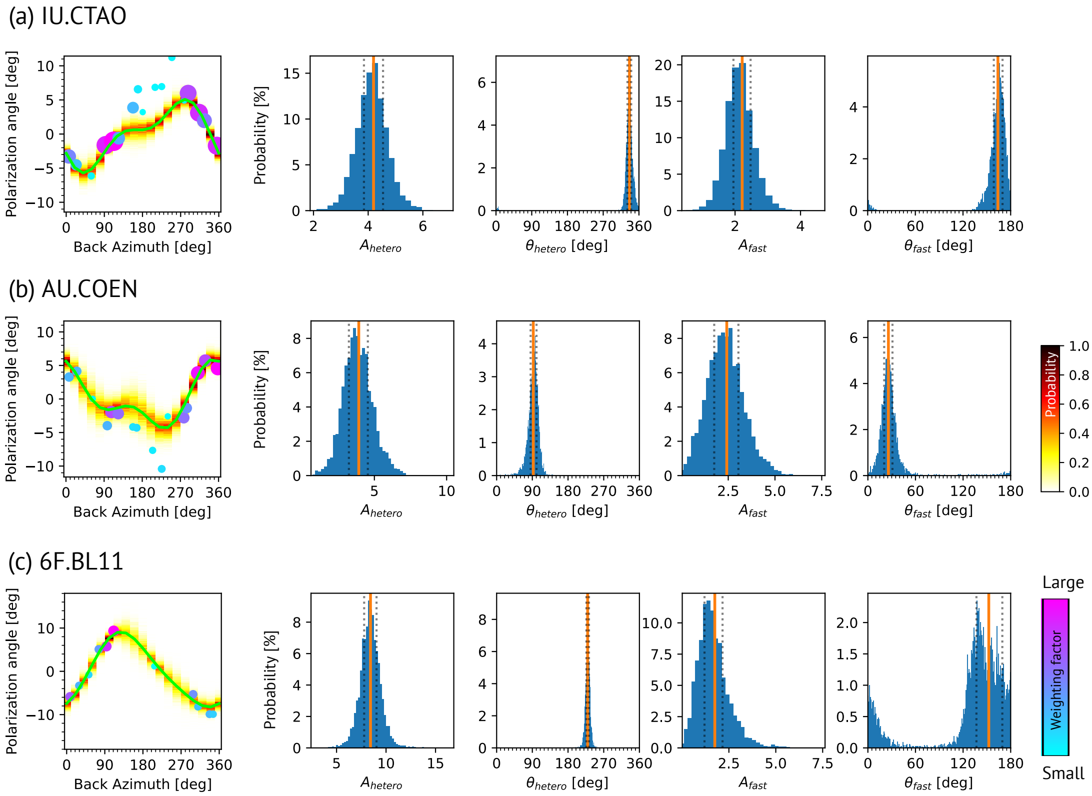

Figure 4: Examples of Bayesian inversion results for three stations dominated by heterogeneity terms (a: IU.CTAO; b: AU.COEN; c: 6F.BL11). For each station, the leftmost panel shows the marginal probability distribution of the predicted data, where the normalized probability is visualized as a heatmap. Green lines denote the mean prediction derived from the ensemble solutions, and the objective data displayed in Figure 2 are overlaid. The remaining panels show posterior histograms of A_{hetero}, θ_{hetero}, A_{fast}, and θ_{fast}. Orange solid lines represent the mean values, and black dotted lines mark the first and third quartiles.

periodicity. At these stations, A_{hetero} is substantially larger than A_{fast}, with the posterior median of A_{hetero} being approximately twice that of A_{fast}.

The inferred positive velocity gradients (Figure 4) are oriented toward the northwest for IU.CTAO (326°; 322°–330°, interquartile range), the east for AU.COEN (91°; 84°–96°), and the west for 6F.BL11 (229°; 225°–232°). For IU.CTAO, the inferred heterogeneity pattern is qualitatively consistent with the deepening direction of the LAB suggested by a receiver function inversion study (Tarumi and Yoshizawa, 2025a). The results for 6F.BL11 are broadly consistent with the velocity-gradient patterns in the upper mantle suggested by recent surface-wave tomography models (e.g., Yoshizawa, 2014; de Laat et al., 2023; Magrini et al., 2023).

On the other hand, the gradient azimuth at AU.COEN differs from the direction of the lateral S-wave velocity decrease in the upper mantle and the deepening of LAB (Yoshizawa, 2014; de Laat et al., 2023). However, it is aligned with the direction of crustal thinning (Kennett et al., 2023), suggesting a possible influence of Moho topography.

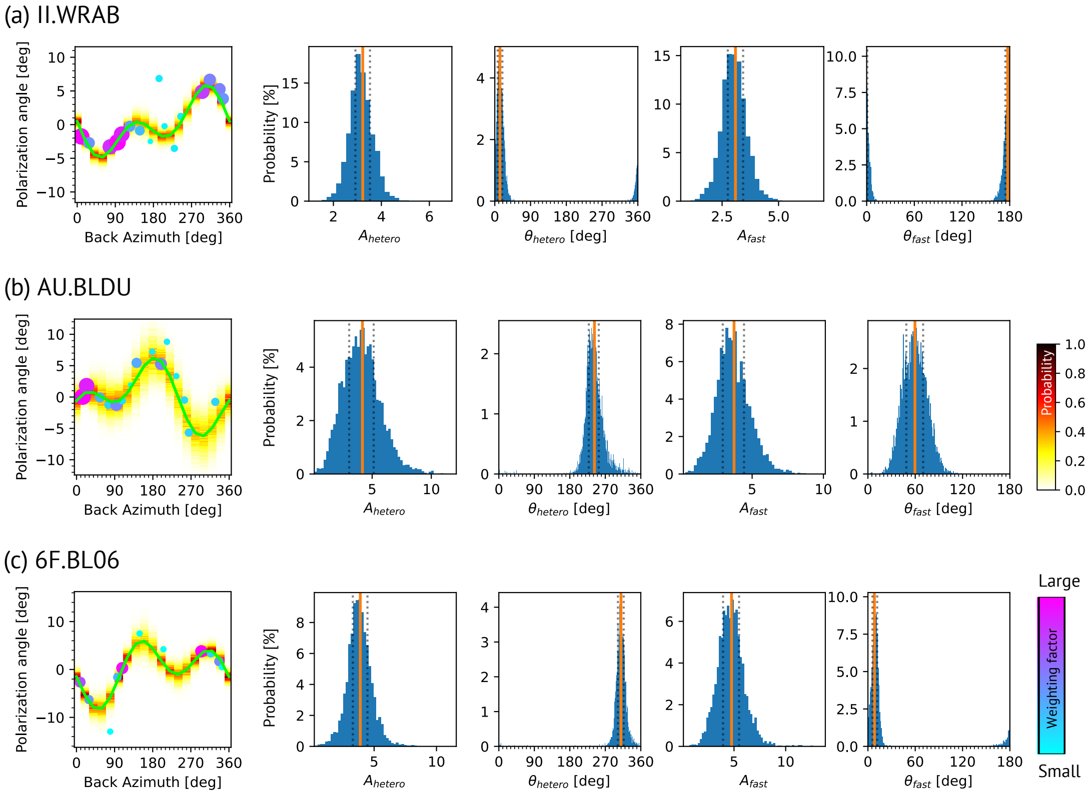

Figure 5: Same as Figure 4, but for three stations dominated by anisotropy terms shown in Figure 3. Notation is the same as Figure 4.

Figure 5 shows the resulting marginal posterior distributions at three stations (a: II.WRAB; b: AU.BLDU; c: 6F.BL06), where the anisotropic components are stronger than the heterogeneity components. For all three stations, the predicted data exhibit clear 2ϕ periodicity, consistent with A_{fast} being larger than A_{hetero}. Overall, the inversion results capture the pronounced azimuthal anisotropy beneath the seismic stations.

At II.WRAB and 6F.BL06 (Figure 5 (a, c)), the fast-axis directions are estimated to be nearly north-south (NS): 178° (174°–182° (i.e., 2°), interquartile range) and 8° (6°–12°), respectively. These estimates are consistent with previous XKS results (Eakin et al., 2021; Ba et al., 2023) and comparable to NS directions inferred from the Rayleigh-wave anisotropy at the asthenospheric depths (100–200 km) (e.g., Simons et al., 2002; Debayle et al., 2005; Fishwick et al., 2008; de Laat et al., 2023). The near north-south orientation is also approximately aligned with absolute plate motion directed to the north-northeast (NNE) (e.g., Argus et al., 2011), suggesting a possible influence from asthenospheric mantle flow. In contrast, at AU.BLDU (Figure 5 (b)), the fast-axis is oriented to the east-northeast (ENE) (71°; 61°–94°), consistent with previous XKS splitting analyses (Chen et al., 2021a; Ba et al., 2023), but not parallel to the absolute plate motion (Argus et al., 2011).

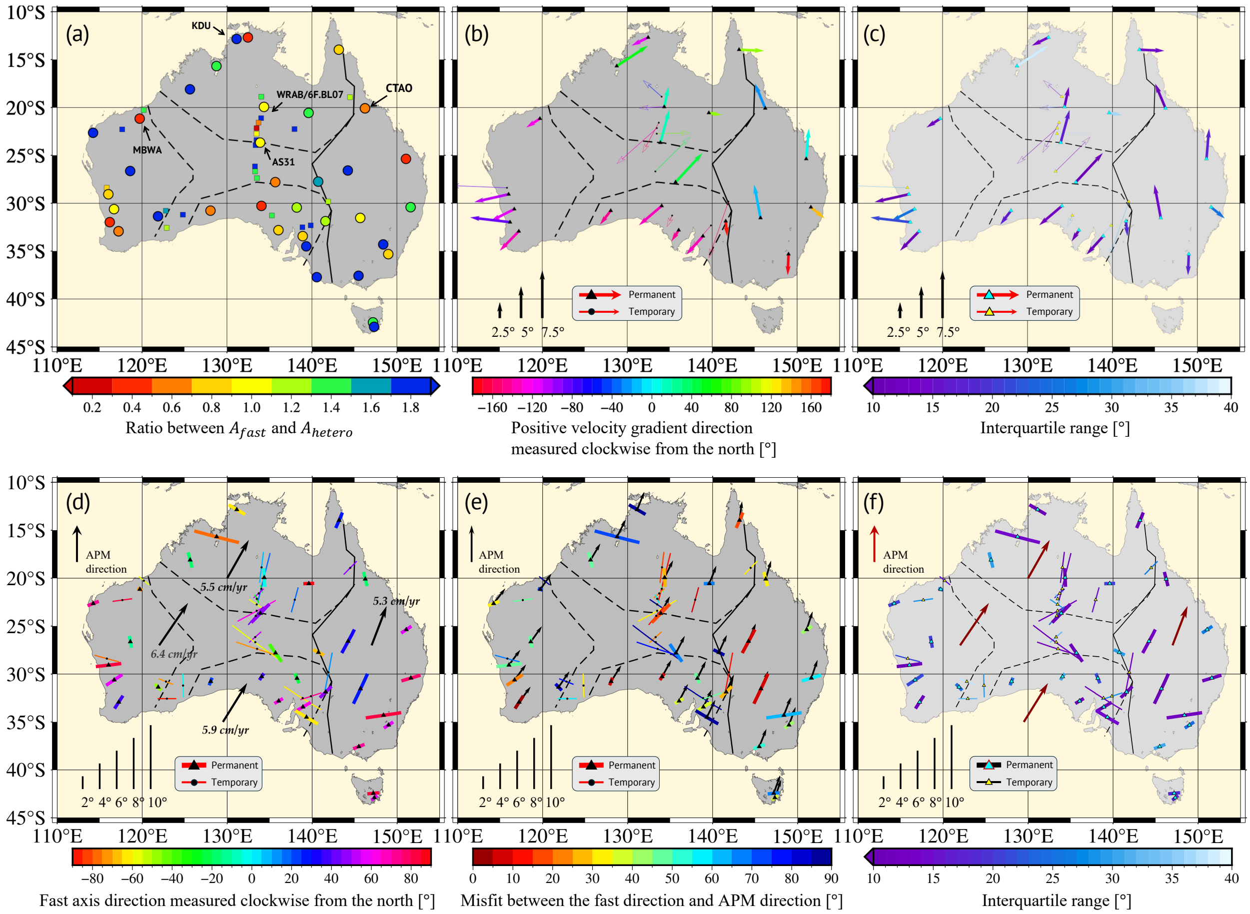

Figure 6: Compilation of Bayesian harmonic analysis results. (a) The magnitude ratio between A_{hetero} and A_{fast}, Δ, which indicates whether anisotropy ($\Delta > 1$) or heterogeneity ($\Delta < 1$) more strongly contributes to the observed polarization anomaly. Large circles and small squares correspond to permanent and temporary stations, respectively. The six representative stations discussed in the text are labeled. (b, c) The positive direction of the velocity gradient θ_{hetero} and its uncertainty quantified by the interquartile range (IQR). Thick and thin arrows correspond to permanent and temporary stations. (d, e, f) The fast-axis direction θ_{fast}, the angular difference between θ_{fast} and the absolute plate motion (APM) direction from Argus et al. (2011), and the IQR of θ_{fast}. Thick and thin bars denote permanent and temporary stations. Black and dark red arrows in (d) and (f) show the APM direction in each tectonic province. Except for (a), black or cyan triangles indicate permanent stations, while black circles in (b, d, e) and yellow triangles in (c, f) indicate temporary stations. The lengths of the arrows or bars (b–f) represent the magnitude of polarization anomaly predicted by the Bayesian inference, while the colors indicate different quantities; (d) fast-axis directions measured from the north, (e) misfit between the fast-axis direction and APM, and (f) uncertainty derived from the IQR.

4.2. Compilations of harmonic analyses

Figure 6 compiles our Bayesian inversion results for all stations. The upper three panels (a–c) show the magnitude ratio between A_{fast} and A_{hetero}, $\Delta \equiv A_{\mathrm{fast}}/A_{\mathrm{hetero}}$, the positive direction of the velocity gradient θ_{hetero}, and its interquartile range (IQR), respectively. The lower panels (d-f) show the inferred fast-axis direction of P-waves, θ_{fast}, the angular difference between the fast-axis and APM (Argus et al., 2011), and the IQR of θ_{fast}, respectively. In this figure, we excluded stations whose directional uncertainties exceed 40° (IQR > 40°).

The uncertainties of θ_{hetero} and θ_{fast}, quantified by the interquartile ranges (IQR), are generally smaller than 20°, indicating that the estimated orientations are reasonably well constrained. These IQRs exhibit no obvious spatial dependence and may instead be controlled by factors such as the number of events and their back-azimuthal distribution. Although the event azimuthal coverage in this study (Figures 1, 2, and 3) may bias the mapping results, the lack of a clear spatial trend in IQR suggests that such biases do not dominantly control the inferred patterns at the regional scale.

As illustrated in Figure 6 (a), larger values of Δ indicate a stronger contribution from azimuthal anisotropy to the teleseismic P-wave polarization anomaly, whereas smaller values ($\Delta < 1$) suggest a stronger contribution from lateral structural heterogeneity. Stations with smaller Δ (< 1) are concentrated in southwestern and northeastern Australia. Relatively small Δ values are also observed in the southern North Australian Craton (NAC) and the South Australian Craton (SAC). In contrast, many inland and southeastern stations exhibit larger Δ, implying that azimuthal anisotropy more strongly contributes to the observed polarization anomalies. Along the continental margin, Δ is typically smaller, likely reflecting lateral variations in crustal or lithospheric thickness.

4.2.1. Lateral heterogeneity

The positive directions of the seismic velocity gradient are displayed in Figure 6(b). Along the continental margin, most stations exhibit broadly similar trends; the inferred direction of increasing P-wave speed is generally oriented seaward from inland areas. In particular, the western and southern margins of Australia show concentrations of westward- and southwestward-trending vectors, respectively (Figure 6 (b)). However, three stations (CTAO, MBWA, and KDU) show opposite orientations directed toward inland regions. These three stations may reflect spatial variations in the depth distribution of lateral heterogeneity, with contributions from structures of different orientations compared to other margin stations, as this dataset reflects path-integrated characters of lateral velocity gradient.

In the inland region, θ_{hetero} shows a complex pattern. While southwestward trends can be identified within the SAC, such trends change remarkably toward tectonic transition zones such as the suture zone or the Phanerozoic Australia (i.e., the Tasman Line). Central Australia exhibits more localized and spatially variable velocity-gradient vectors. WRAB and AS31 show comparable NNE-oriented gradients, whereas nearby temporary stations indicate contrasting patterns, possibly suggesting the localized lateral heterogeneity around the southern NAC. Although the 6F.BL07 station (Rawlinson and Kennett, 2008) is very close to the permanent station of WRAB, the resultant directions are nearly perpendicular to each other, which may be related to the number and azimuthal coverage of the events used in this analysis.

4.2.2. *Azimuthal anisotropy*

The azimuthal anisotropy mapped in Figure 6 (d, e) shows clear spatial variations that correlate with the tectonic setting of Australia. In eastern Phanerozoic Australia, the fast-axis directions are predominantly northward and are broadly consistent with the APM direction (Argus et al., 2011), especially near the transition zone with the SAC. In contrast, across the transition between the suture zone and adjacent regions, the fast axes are nearly perpendicular to the APM. Farther south, including Tasmania, the fast-axis rotates toward an ENE–WSW trend and deviates from the APM direction.

In the cratonic regions, the azimuthal anisotropy varies among individual cratonic blocks and adjacent regions. In the SAC, ENE–WSW trends are dominantly observed, with some local variations. Several stations between the suture zone and the SAC show ESE–WNW orientations, and the fast-axis direction rapidly changes in the northern areas. At the margin between the NAC and the suture zone, NE–SW trends are observed. Within the BILBY array (Rawlinson and Kennett, 2008) in central Australia, the fast-axis pattern varies in a complex manner and becomes aligned with APM toward the northern end. The fast-axes tend to trend SE–NW in the Musgrave Province and nearly N–S in the Albany–Fraser Orogen. The northern and eastern NAC contrast with the southern NAC, showing nearly E–W fast-axis directions. At the margin between the WAC and the suture zone, SE–NW trends are observed and are nearly perpendicular to APM (Argus et al., 2011). In contrast, the western margin of the WAC exhibits predominantly ENE–WSW to E–W trends.

5. Discussion

The results in the previous section reveal systematic spatial variations in both lateral velocity gradients and azimuthal anisotropy across Australia (Figure 6), with clear dependence on tectonic setting. The relative dominance of lateral heterogeneity and azimuthal anisotropy, quantified by Δ, also varies regionally and may provide additional constraints on the origin of the observed signals.

In this section, we first discuss possible causes of the ϕ-term in Equation (2), focusing on Moho and LAB topography. We then compare our results with previous XKS splitting analyses (Chen et al., 2021a; Eakin et al., 2021, 2023; Ba et al., 2023) and tomographic models (e.g., Debayle and Kennett, 2000; Simons et al., 2002; Debayle et al., 2016; Pilia et al., 2016; de Laat et al., 2023) to explore the origin of the inferred azimuthal anisotropy.

5.1. Lateral heterogeneity

Lateral velocity gradients in the crust and upper mantle can arise from topography of major interfaces such as the Moho and the lithosphere-asthenosphere boundary (LAB), as well as from velocity variations within the

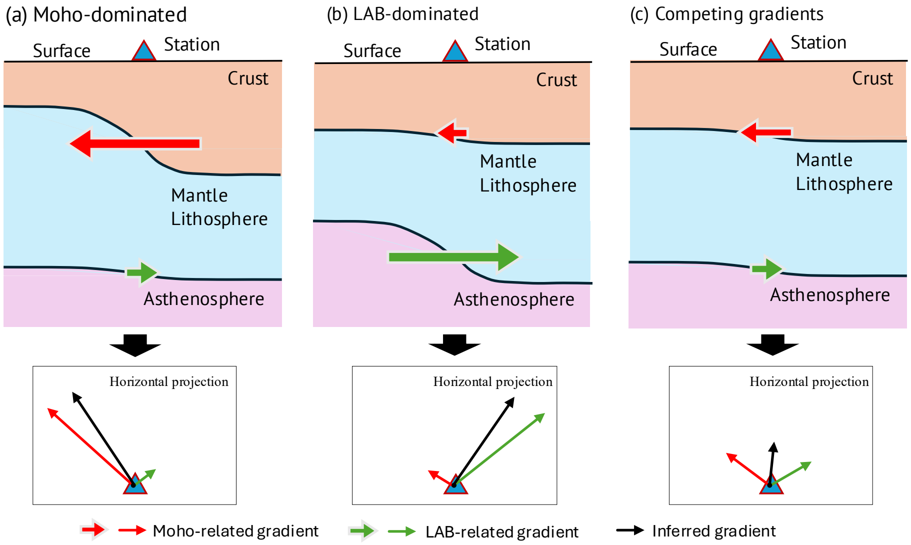

Figure 7: Schematic illustration showing how lateral velocity gradients at different depths contribute to teleseismic P-wave polarization anomalies. Moho and LAB topography are shown as representative sources of strong lateral velocity gradients, although gradients within the lithosphere may also contribute. (a) Moho-dominated case. (b) LAB-dominated case. (c) Competing case, where the observed polarization direction reflects contributions from both the Moho- and LAB-related velocity gradients. Because teleseismic P-waves have depth-dependent sensitivity, the observed polarization direction reflects the relative contributions of velocity gradients at different depths rather than a simple vector sum.

lithosphere (Figure 7). The observed P-wave polarization anomalies can be influenced by these gradients, and the inferred directions should be interpreted as reflecting their relative contributions.

Most stations along the continental margin show a common pattern in which the velocity-gradient vectors are oriented seaward (Figure 6 (b, c)), consistent with crustal thinning from inland regions toward the ocean. This pattern agrees with the AusMoho model, which indicates that the Moho generally deepens from the continental margin toward central Australia (Kennett et al., 2023). In central Australia, where the Moho exhibits complex topography (Kennett et al., 2023), the velocity-gradient patterns are correspondingly more variable (Figure 6 (b, c)).

In contrast, the velocity-gradient directions at CTAO, KDU, and MBWA are not oriented seaward. Previous studies have suggested localized variations in lithospheric thickness beneath northern and northeastern Australia (e.g., Kennett et al., 2013; Yoshizawa, 2014), as well as northwestward LAB deepening beneath CTAO Tarumi and Yoshizawa (2025a). These observations suggest that the inferred gradients at these stations may reflect localized lithospheric structure, including variations in LAB depth, rather than the large-scale Moho topography observed along the continental margin.

5.2. Comparison with previous studies

This paper presents the spatial distribution of azimuthal anisotropy inferred from teleseismic P-wave polarization anomalies (Figure 6 (d–f)). Previous studies have also extracted azimuthal anisotropy from P-wave polarization data (Schulte-Pelkum et al., 2001; Fontaine et al., 2009), although differences exist at some stations. For example, our result for IU.NWAO is consistent with Fontaine et al. (2009) but nearly perpendicular to that of Schulte-Pelkum et al. (2001), likely reflecting differences in data coverage and inversion methodology.

In addition, XKS splitting has been widely used to investigate seismic anisotropy across Australia (Vinnik et al., 1992; Heintz and Kennett, 2005; Bello et al., 2019; Eakin et al., 2021; Ba et al., 2023; Eakin et al., 2023; Birkey and Ford, 2023; Gauntlett et al., 2025). Figure S3 compares the fast-axis directions from this study with those from recent XKS studies at same stations (Eakin et al., 2021, 2023; Ba et al., 2023; Birkey and Ford, 2023). Overall, our inferred fast-axis patterns are broadly consistent with previously reported S-wave anisotropy, although some regional discrepancies remain.

The main similarities are observed at the scale of major tectonic provinces. In eastern Phanerozoic Australia, the fast-axis directions are predominantly aligned with the APM trend (Figure 6 (e)) and are broadly consistent with both XKS splitting results (Eakin et al., 2023; Ba et al., 2023; Birkey and Ford, 2023) (Figure S3) and Rayleigh-wave anisotropy models (Simons et al., 2002; Fishwick et al., 2008; de Laat et al., 2023). In parts of cratonic Australia, including the western WAC and portions of the SAC, the inferred fast-axis trends are also broadly compatible with previously reported anisotropic patterns from XKS splitting (Chen et al., 2021a; Eakin et al., 2021; Ba et al., 2023; Birkey and Ford, 2023; Gauntlett et al., 2025). These similarities suggest that P-wave polarization anomalies capture first-order regional anisotropic fabrics.

Noticeable differences are concentrated around the suture zone (including the eastern Musgrave and Albany–Fraser Orogen) and in southeastern Australia. In these regions, the inferred fast-axis directions locally deviate from XKS splitting, even where neighboring stations show coherent patterns in our analysis. Such discrepancies may reflect differences in depth sensitivity and sampling geometry among teleseismic P-wave polarization, XKS splitting, and surface-wave tomography (Schulte-Pelkum et al., 2001). In particular, teleseismic P-wave polarization anomalies sample laterally offset regions compared to XKS phases, which primarily probe structure directly beneath the receiver (Figure S2).

5.3. Implications for Anisotropy

Having summarized the similarities and differences between our P-wave-based anisotropy and previously reported S-wave anisotropy patterns, we now discuss possible interpretations of the inferred anisotropic structures. Surface-wave (SW) tomography provides constraints on large-scale azimuthal anisotropic pattern with improved vertical resolution (e.g., de Laat et al., 2023). Comparison with these models offer a useful framework for assessing the relative contributions of lithospheric and asthenospheric anisotropy.

5.3.1. Eastern Phanerozoic Australia

In eastern Phanerozoic Australia, the fast-axis directions are generally aligned with the APM direction (Argus et al., 2011) in the northern and central regions (Figure 6 (d–f)). This pattern is consistent with NE-SW anisotropic trends at asthenospheric depths imaged by regional and global Rayleigh-wave models (Simons et al., 2002; Fishwick et al., 2008; de Laat et al., 2023; Debayle et al., 2016). These observations suggest that the inferred P-wave anisotropy is significantly influenced by present-day asthenospheric mantle flow.

In contrast, southeastern Australia shows larger deviations from APM, with fast-axis directions rotating toward E-W (Figure 6 (d–f)). These deviations may reflect spatially variable mantle flow and/or changes in the relative contribution of lithospheric and asthenospheric anisotropy. Dynamic mantle-flow modeling (Eakin et al., 2023) has demonstrated that localized asthenospheric flow anomalies can perturb XKS splitting patterns in this region. The observed transitions in fast-axis directions in this study suggest that the similar processes may influence the P-wave polarization results.

The Phanerozoic province is also characterized by relatively thin lithosphere (∼100 km; e.g., Kennett et al., 2013; Magrini et al., 2023). In such regions, where lithospheric anisotropy may be less dominant, seismic anisotropy is more likely to reflect asthenospheric mantle flow (e.g., Vinnik et al., 1992). This interpretation is consistent with XKS splitting results, which show fast-axis directions aligned with the mantle flow (Eakin et al., 2023). Together, these observations suggest that both P- and S-wave anisotropy in eastern Australia are strongly influenced by asthenospheric flow beneath a relatively thin lithosphere.

5.3.2. Cratonic Australia

Cratonic Australia is characterized by thick lithosphere (typically 120–200 km), with locally thicker regions (up to ∼220 km) beneath parts of the suture zone and central Australia (e.g., Kennett et al., 2013; Yoshizawa, 2014; Magrini et al., 2023; Tarumi and Yoshizawa, 2025b). In these regions, the inferred fast-axis directions commonly deviate from the APM direction (Figure 6 (d–f)), suggesting that the observed anisotropy is not primarily controlled by present-day asthenospheric flow, in contrast to eastern Phanerozoic Australia. Instead, the large-scale patterns are more plausibly explained by lithospheric frozen anisotropy inherited from ancient tectonic processes.

In the SAC, especially in the eastern SAC including the Gawler Craton, the dominant NE-SW fast-axis trend may reflect lithospheric fabrics associated with Proterozoic deformation. The regional tectonic history includes major NW-SE compression around 1.6 Ga, documented by E-W to NE-SW structural trends (Hand et al., 2007), and the inferred anisotropy may preserve this tectonic imprint.

In the WAC, the fast-axis directions show predominantly E-W trends in the western coastal region. These results are consistent with anisotropy inferred at ∼80km depths from P-wave receiver function analysis (Chen et al., 2021b), suggesting a lithospheric origin. Recent higher-resolution XKS studies Gauntlett et al. (2025) also indicate a correlation with Archean dyke orientations (∼2 Ga; e.g., Liu et al., 2019; Aitken et al., 2023), supporting their influence on observed anisotropy. Alternative interpretations, such as the edge-driven convection related to LAB topography Birkey and Ford (2023), have been proposed, but are not fully consistent with surface-wave models (e.g., de Laat et al., 2023). Overall, the depth-integrated anisotropy inferred from both P-wave polarization anomalies and XKS splitting is more plausibly attributed to lithospheric structures formed during ancient tectonic processes rather than to present-day mantle flow.

Near the margin between the WAC and the suture zone, NW-SE to WNW-ESE trends are observed in central to eastern regions. Such rapid spatial variations are likely related to the tectonic boundaries and may reflect inherited structures associated with Proterozoic cratonic amalgamation (1.6–1.0 Ga; Myers, 1993).

The NAC exhibits contrasting characteristics between its northwestern and southern parts. The northwestern NAC shows WNW-ESE anisotropy, consistent with Rayleigh-wave anisotropy within the lithosphere down to 80 km (Debayle et al., 2016; de Laat et al., 2023). In contrast, the southern NAC is characterized by near N–S fast-axis directions, aligned with the APM direction (Argus et al., 2011). Because Rayleigh-wave models indicate that azimuthal anisotropy in the asthenosphere (150–300 km) is mostly oriented N–S or NNE–SSW (Simons et al., 2002; Fishwick et al., 2008; Debayle et al., 2016; de Laat et al., 2023), the inferred P-wave anisotropy in the southern NAC may reflect this anisotropic pattern. In contrast, the lithospheric anisotropy exhibits different orientations (Simons et al., 2002; Fishwick et al., 2008; Debayle et al., 2016; de Laat et al., 2023). Nevertheless, the depth-integrated anisotropy appear to correlate with the APM direction (Figure 6 (d–f); Eakin et al., 2021; Ba et al., 2023; Birkey and Ford, 2023), which likely indicate a strong influence of asthenospheric shear flow or basal drag beneath the southern NAC.

Anisotropy in the central Australian suture zone is particularly complex and varies over short spatial scales, as illustrated by the dense BILBY array (Rawlinson and Kennett, 2008) and surrounding stations. This spatial variability likely reflects superposed tectonic fabrics associated with cratonic amalgamation and subsequent reactivation. The inferred P-wave fast-axis directions are consistent with crustal deformation related to the the Alice Springs Orogeny (ca. 400 Ma; Klootwijk, 2013) and are broadly comparable with lithospheric anisotropy inferred from previous tomographic models (Simons et al., 2002; Debayle et al., 2016; de Laat et al., 2023). In addition, the central suture zone (e.g., the Musgrave Orogen) has experienced multiple episodes of crustal reworking (Kennett and Iaffaldano, 2013), likely contributing to complex lithospheric structure and Moho topography (Kennett et al., 2023). Such structural complexity may also be reflected in the lateral velocity gradients inferred from P-wave polarization anomalies (Figure 6 (b, c) and Section 5.1). Overall, the fast-axis patterns in central Australia likely record inherited anisotropy associated with ancient tectonic processes, including cratonic amalgamation and the subsequent orogenic events.

6. Conclusions

In this study, we estimated the lateral velocity gradients and azimuthal anisotropy of P-waves beneath the Australian continent using teleseismic P-wave polarization anomalies recorded at permanent and temporary seismic stations. The inferred fast-propagation directions generally correlate with the direction of crustal thinning along continental margins, while some stations indicate the influence of localized variations in lithospheric thickness.

The spatial distribution of fast-axis orientations varies systematically among tectonic provinces. In eastern Phanerozoic Australia and parts of the southern NAC, the observed anisotropy is consistent with present-day asthenospheric mantle flow. In contrast, much of cratonic Australia exhibits anisotropic patterns that are more plausibly attributed to lithospheric frozen anisotropy inherited from ancient tectonic processes.

These results demonstrate that teleseismic P-wave polarization anomalies provide a useful complementary constraint on upper-mantle anisotropy beneath continents. Future studies should integrate this approach with other seismic observations, including surface-wave tomography and receiver-function analyses (e.g., Tarumi and Yoshizawa, 2025a), as well as azimuth-dependent P-wave receiver functions (e.g., Chen et al., 2021b), to better resolve depth-dependent and laterally variable anisotropic structures and to improve our understanding of continental evolution.

Acknowledgments

This study was partly supported by JST SPRING (grant number JPMJSP2119 to KT) and JSPS KAKENHI (grant numbers 24KJ0294 to KT; 23K03539 to KY).

Data and code availability

All seismograms used in this study were downloaded from the IRIS Data Management Center (https://ds.iris.edu/ds/nodes/dm We used ObsPy (Beyreuther et al., 2010) for downloading and analyzing all seismic waveform data, and generated all figures using matplotlib (Hunter, 2007), Generic Mapping Tools (Wessel et al., 2019), and PyGMT (Uieda et al., 2021).

Competing interests

The authors declare that they have no competing interests.

Author Contribution

Kotaro Tarumi: Conceptualization; Data curation; Methodology; Formal analysis; Funding acquisition; Investigation; Visualization; Software; Project administration; Writing- Original draft preparation

Kazunori Yoshizawa: Conceptualization; Data curation; Methodology; Funding acquisition; Investigation; Project administration; Writing- reviewing and editing

References

O. Abril-Pla, V. Andreani, C. Carroll, L. Dong, C. J. Fonnesbeck, M. Kochurov, R. Kumar, J. Lao, C. C. Luhmann, O. A. Martin, M. Osthege, R. Vieira, T. Wiecki, R. Zinkov, PyMC: a modern, and comprehensive probabilistic programming framework in Python, PeerJ Computer Science 9 (2023) e1516. doi:10.7717/peerj-cs.1516.

A. Aitken, M. Fiorentini, M. Tesauro, N. Thébaud, Supercontinent-paced magmatic destabilisation and recratonisation of the Yilgarn Craton, Gondwana Research 116 (2023) 12–24. doi:10.1016/j.gr.2022.11.016.

D. F. Argus, R. G. Gordon, C. DeMets, Geologically current motion of 56 plates relative to the no-net-rotation reference frame, Geochemistry, Geophysics, Geosystems 12 (2011) n/a–n/a. doi:10.1029/2011gc003751.

K. Ba, S. S. Gao, J. Song, K. H. Liu, Seismic Azimuthal Anisotropy Beneath a Fast Moving Ancient Continent: Constraints From Shear Wave Splitting Analysis in Australia, Journal of Geophysical Research: Solid Earth 128 (2023). doi:10.1029/2022jb025866.

M. Bello, D. Cornwell, N. Rawlinson, A. Reading, Insights into the structure and dynamics of the upper mantle beneath Bass Strait, southeast Australia, using shear wave splitting, Physics of the Earth and Planetary Interiors 289 (2019) 45–62. doi:10.1016/j.pepi.2019.02.002.

M. Beyreuther, R. Barsch, L. Krischer, T. Megies, Y. Behr, J. Wassermann, ObsPy: A Python Toolbox for Seismology, Seismological Research Letters 81 (2010) 530–533. doi:10.1785/gssrl.81.3.530.

A. Birkey, H. A. Ford, Anisotropic structure of the Australian continent, Frontiers in Earth Science 10 (2023) 1055480. doi:10.3389/feart.2022.1055480.

A. Birkey, H. A. Ford, P. Dabney, G. Goldhagen, The Lithospheric Architecture of Australia From Seismic Receiver Functions, Journal of Geophysical Research: Solid Earth 126 (2021). doi:10.1029/2020jb020999.

X. Chen, V. Levin, H. Yuan, Small Shear Wave Splitting Delays Suggest Weak Anisotropy in Cratonic Mantle Lithosphere, Geophysical Research Letters 48 (2021a). doi:10.1029/2021gl093861.

X. Chen, V. Levin, H. Yuan, M. Klaser, Y. Li, Seismic Anisotropic Layering in the Yilgarn and Superior Cratonic Lithosphere, Journal of Geophysical Research: Solid Earth 126 (2021b). doi:10.1029/2020jb021575.

S. Crampin, R. A. Stephen, R. McGonigle, The polarization of P-waves in anisotropic media, Geophysical Journal of the Royal Astronomical Society 68 (1982) 477–485. doi:10.1111/j.1365-246x.1982.tb04910.x.

L. Cristiano, T. Meier, F. Krüger, H. Keers, C. Weidle, Teleseismic P -wave polarization analysis at the Gräfenberg array, Geophysical Journal International 207 (2016) 1456–1471. doi:10.1093/gji/ggw339.

D. R. Davies, N. Rawlinson, G. Iaffaldano, I. H. Campbell, Lithospheric controls on magma composition along Earth's longest continental hotspot track, Nature 525 (2015) 511–514. doi:10.1038/nature14903.

E. Debayle, F. Dubuffet, S. Durand, An automatically updated S-wave model of the upper mantle and the depth extent of azimuthal anisotropy, Geophysical Research Letters 43 (2016) 674–682. doi:10.1002/2015gl067329.

E. Debayle, B. Kennett, K. Priestley, Global azimuthal seismic anisotropy and the unique plate-motion deformation of Australia, Nature 433 (2005) 509–512. doi:10.1038/nature03247.

E. Debayle, B. L. N. Kennett, The Australian continental upper mantle: Structure and deformation inferred from surface waves, Journal of Geophysical Research: Solid Earth 105 (2000) 25423–25450. doi:10.1029/2000jb900212.

J. I. de Laat, S. Lebedev, N. L. Celli, R. Bonadio, B. Chagas de Melo, N. Rawlinson, Structure and evolution of the Australian plate and underlying upper mantle from waveform tomography with massive data sets, Geophysical Journal International 234 (2023) 153–189. doi:10.1093/gji/ggad062.

C. M. Eakin, D. R. Davies, S. Ghelichkhan, J. P. O'Donnell, S. Agrawal, The Influence of Lithospheric Thickness Variations Beneath Australia on Seismic Anisotropy and Mantle Flow, Geochemistry, Geophysics, Geosystems 24 (2023). doi:10.1029/2023gc011066.

C. M. Eakin, C. Flashman, S. Agrawal, Seismic anisotropy beneath Central Australia: A record of ancient lithospheric deformation, Tectonophysics 820 (2021) 229123. doi:10.1016/j.tecto.2021.229123.

S. Fishwick, M. Heintz, B. L. N. Kennett, A. M. Reading, K. Yoshizawa, Steps in lithospheric thickness within eastern Australia, evidence from surface wave tomography, Tectonics 27 (2008) n/a–n/a. doi:10.1029/2007tc002116.

F. R. Fontaine, G. Barruol, B. L. N. Kennett, G. H. R. Bokelmann, D. Reymond, Upper mantle anisotropy beneath Australia and Tahiti from P wave polarization: Implications for real-time earthquake location, Journal of Geophysical Research: Solid Earth 114 (2009). doi:10.1029/2008jb005709.

H. A. Ford, K. M. Fischer, D. L. Abt, C. A. Rychert, L. T. Elkins-Tanton, The lithosphere–asthenosphere boundary and cratonic lithospheric layering beneath Australia from Sp wave imaging, Earth and Planetary Science Letters 300 (2010) 299–310. doi:10.1016/j.epsl.2010.10.007.

A. W. Frederiksen, M. G. Bostock, Modelling teleseismic waves in dipping anisotropic structures, Geophysical Journal International 141 (2000) 401–412. doi:10.1046/j.1365-246x.2000.00090.x.

M. Gauntlett, C. M. Eakin, N. Bishoyi, P. Zhang, J. O'Donnell, R. E. Murdie, M. S. Miller, R. Pickle, R. Ebrahimi, Seismic Anisotropy Analysis Across Southwestern Australia Reveals ENE-Trending Lithospheric Architecture Linked to Archean Yilgarn Craton Formation, Geochemistry, Geophysics, Geosystems 26 (2025). doi:10.1029/2025gc012589.

R. A. Glen, The Tasmanides of eastern Australia, Geological Society, London, Special Publications 246 (2005) 23–96. doi:10.1144/gsl.sp.2005.246.01.02.

M. Hand, A. Reid, L. Jagodzinski, Tectonic Framework and Evolution of the Gawler Craton, Southern Australia, Economic Geology 102 (2007) 1377–1395. doi:10.2113/gsecongeo.102.8.1377.

M. Heintz, B. L. Kennett, Continental scale shear wave splitting analysis: Investigation of seismic anisotropy underneath the Australian continent, Earth and Planetary Science Letters 236 (2005) 106–119. doi:10.1016/j.epsl.2005.05.003.

J. D. Hunter, Matplotlib: A 2D Graphics Environment, Computing in Science & Engineering 9 (2007) 90–95. doi:10.1109/mcse.2007.55.

M. Ishise, A. Kato, S. Sakai, S. Nakagawa, N. Hirata, Improved 3-D P Wave Azimuthal Anisotropy Structure Beneath the Tokyo Metropolitan Area, Japan: New Interpretations of the Dual Subduction System Revealed by Seismic Anisotropy, Journal of Geophysical Research: Solid Earth 126 (2021). doi:10.1029/2020jb021194.

B. Kennett, G. Iaffaldano, Role of lithosphere in intra-continental deformation: Central Australia, Gondwana Research 24 (2013) 958–968. doi:10.1016/j.gr.2012.10.010.

B. L. N. Kennett, A. Fichtner, S. Fishwick, K. Yoshizawa, Australian Seismological Reference Model (AuSREM): mantle component, Geophysical Journal International 192 (2013) 871–887. doi:10.1093/gji/ggs065.

B. L. N. Kennett, A. Gorbatov, H. Yuan, S. Agrawal, R. Murdie, M. P. Doublier, C. M. Eakin, M. S. Miller, L. Zhao, K. Czarnota, J. P. O'Donnell, M. Dentith, K. Gessner, Refining the Moho across the Australian continent, Geophysical Journal International 233 (2023) 1863–1877. doi:10.1093/gji/ggad035.

C. Klootwijk, Middle–Late Paleozoic Australia–Asia convergence and tectonic extrusion of Australia, Gondwana Research 24 (2013) 5–54. doi:10.1016/j.gr.2012.10.007.

X. Liu, D. Zhao, Seismic velocity azimuthal anisotropy of the Japan subduction zone: Constraints from P and S wave traveltimes, Journal of Geophysical Research: Solid Earth 121 (2016) 5086–5115. doi:10.1002/2016jb013116.

Y. Liu, Z.-X. Li, S. Pisarevsky, U. Kirscher, R. N. Mitchell, J. C. Stark, Palaeomagnetism of the 1.89 Ga Boonadgin dykes of the Yilgarn Craton: Possible connection with India, Precambrian Research 329 (2019) 211–223. doi:10.1016/j.precamres.2018.05.021.

F. Magrini, E. Kästle, S. Pilia, N. Rawlinson, L. Siena, A New Shear-Velocity Model of Continental Australia Based on Multi-Scale Surface-Wave Tomography, Journal of Geophysical Research: Solid Earth 128 (2023). doi:10.1029/2023jb026688.

V. Maupin, J. Park, Treatise on Geophysics (Second Edition) (2015) 277–305. doi:10.1016/b978-0-444-53802-4.00007-5.

J. Montagner, T. Tanimoto, Global anisotropy in the upper mantle inferred from the regionalization of phase velocities, Journal of Geophysical Research: Solid Earth 95 (1990) 4797–4819. doi:10.1029/jb095ib04p04797.

J. Montagner, T. Tanimoto, Global upper mantle tomography of seismic velocities and anisotropies, Journal of Geophysical Research: Solid Earth 96 (1991) 20337–20351. doi:10.1029/91jb01890.

J. S. Myers, Precambrian History of the West Australian Craton and Adjacent Orogens, Annual Review of Earth and Planetary Sciences 21 (1993) 453–485. doi:10.1146/annurev.ea.21.050193.002321.

J. S. Myers, R. D. Shaw, I. M. Tyler, Tectonic evolution of Proterozoic Australia, Tectonics 15 (1996) 1431–1446. doi:10.1029/96tc02356.

S. Pilia, P. Arroucau, N. Rawlinson, A. M. Reading, R. A. Cayley, Inherited crustal deformation along the East Gondwana margin revealed by seismic anisotropy tomography, Geophysical Research Letters 43 (2016) 12,082–12,090. doi:10.1002/2016gl071201.

N. Rawlinson, M. Salmon, B. Kennett, Transportable seismic array tomography in southeast Australia: Illuminating the transition from Proterozoic to Phanerozoic lithosphere, Lithos 189 (2014) 65–76. doi:10.1016/j.lithos.2013.06.001.

S. Rawlinson, B. Kennett, BILBY, 2008. URL: https://www.fdsn.org/networks/detail/6F_2008/.

V. Schulte-Pelkum, D. K. Blackman, A synthesis of seismic P and S anisotropy, Geophysical Journal International 154 (2003) 166–178. doi:10.1046/j.1365-246x.2003.01951.x.

V. Schulte-Pelkum, G. Masters, P. M. Shearer, Upper mantle anisotropy from long-period P polarization, Journal of Geophysical Research: Solid Earth 106 (2001) 21917–21934. doi:10.1029/2001jb000346.

F. J. Simons, R. D. V. D. Hilst, J. Montagner, A. Zielhuis, Multimode Rayleigh wave inversion for heterogeneity and azimuthal anisotropy of the Australian upper mantle, Geophysical Journal International 151 (2002) 738–754. doi:10.1046/j.1365-246x.2002.01787.x.

W. Sun, B. L. N. Kennett, Uppermost mantle structure of the Australian continent from Pn traveltime tomography, Journal of Geophysical Research: Solid Earth 121 (2016) 2004–2019. doi:10.1002/2015jb012597.

T. Tanimoto, D. L. Anderson, Lateral heterogeneity and azimuthal anisotropy of the upper mantle: Love and Rayleigh waves 100–250 s, Journal of Geophysical Research: Solid Earth 90 (1985) 1842–1858. doi:10.1029/jb090ib02p01842.

K. Tarumi, K. Yoshizawa, Detecting rapid lateral changes of upper mantle discontinuities using azimuth-dependent P-wave receiver functions and multimode surface waves, Physics of the Earth and Planetary Interiors (2025a) 107468. doi:10.1016/j.pepi.2025.107468.

K. Tarumi, K. Yoshizawa, Mapping upper mantle discontinuities beneath the Australian continent using multimode surface waves and receiver functions (2025b). doi:10.31223/x54j05.

K. Tarumi, K. Yoshizawa, Station-Orientation Catalog for Australian Broadband Seismic Stations, Pure and Applied Geophysics (2025c). doi:10.1007/s00024-025-03827-7.

L. Uieda, D. Tian, W. J. Leong, M. Jones, W. Schlitzer, L. Toney, M. Grund, J. Yao, Y. Magen, K. Materna, T. Newton, A. Anant, M. Ziebarth, P. Wessel, J. Quinn, PyGMT: A Python interface for the Generic Mapping Tools (2021). doi:10.5281/zenodo.5607255.

J. Veevers, Gondwanaland from 650–500 Ma assembly through 320 Ma merger in Pangea to 185–100 Ma breakup: supercontinental tectonics via stratigraphy and radiometric dating, Earth-Science Reviews 68 (2004) 1–132. doi:10.1016/j.earscirev.2004.05.002.

L. P. Vinnik, L. I. Makeyeva, A. Milev, A. Y. Usenko, Global patterns of azimuthal anisotropy and deformations in the continental mantle, Geophysical Journal International 111 (1992) 433–447. doi:10.1111/j.1365-246x.1992.tb02102.x.

P. Wessel, J. F. Luis, L. Uieda, R. Scharroo, F. Wobbe, W. H. F. Smith, D. Tian, The Generic Mapping Tools Version 6, Geochemistry, Geophysics, Geosystems 20 (2019) 5556–5564. doi:10.1029/2019gc008515.

J. Wolf, T. W. Becker, E. Garnero, K. H. Liu, J. D. West, Comprehensive global data set of uniformly processed shear-wave splitting measurements, Geophysical Journal International 241 (2025) 863–875. doi:10.1093/gji/ggaf076.

A. Wüstefeld, G. Bokelmann, G. Barruol, J.-P. Montagner, Identifying global seismic anisotropy patterns by correlating shear-wave splitting and surface-wave data, Physics of the Earth and Planetary Interiors 176 (2009) 198–212. doi:10.1016/j.pepi.2009.05.006.

M. Yoshida, Dynamic role of the rheological contrast between cratonic and oceanic lithospheres in the longevity of cratonic lithosphere: A three-dimensional numerical study, Tectonophysics 532 (2012) 156–166. doi:10.1016/j.tecto.2012.01.029.

M. Yoshida, K. Yoshizawa, Continental Drift with Deep Cratonic Roots, Annual Review of Earth and Planetary Sciences 49 (2020) 1–23. doi:10.1146/annurev-earth-091620-113028.

K. Yoshizawa, Radially anisotropic 3-D shear wave structure of the Australian lithosphere and asthenosphere from multi-mode surface waves, Physics of the Earth and Planetary Interiors 235 (2014) 33–48. doi:10.1016/j.pepi.2014.07.008.

K. Yoshizawa, B. L. N. Kennett, Multimode surface wave tomography for the Australian region using a three-stage approach incorporating finite frequency effects, Journal of Geophysical Research: Solid Earth 109 (2004). doi:10.1029/2002jb002254.

K. Yoshizawa, B. L. N. Kennett, The lithosphere-asthenosphere transition and radial anisotropy beneath the Australian continent, Geophysical Research Letters 42 (2015) 3839–3846. doi:10.1002/2015gl063845.

H. Yuan, B. Romanowicz, Lithospheric layering in the North American craton, Nature 466 (2010) 1063–1068. doi:10.1038/nature09332.

S. Özalaybey, W.-P. Chen, Frequency-dependent analysis of SKS/SKKS waveforms observed in Australia: evidence for null birefringence, Physics of the Earth and Planetary Interiors 114 (1999) 197–210. doi:10.1016/s0031-9201(99)00058-8.

Supplementary Material for

Azimuthal Anisotropy and Lateral Heterogeneity Beneath Australia From Teleseismic P-wave Polarization Anomalies

K. Tarumi[1,*] and K. Yoshizawa[1]

[1] Department of Earth & Planetary Sciences, Faculty of Science, Hokkaido University, Sapporo 060-0810, Japan.

[*]Corresponding author: tarumi.kotaro.jp@gmail.com

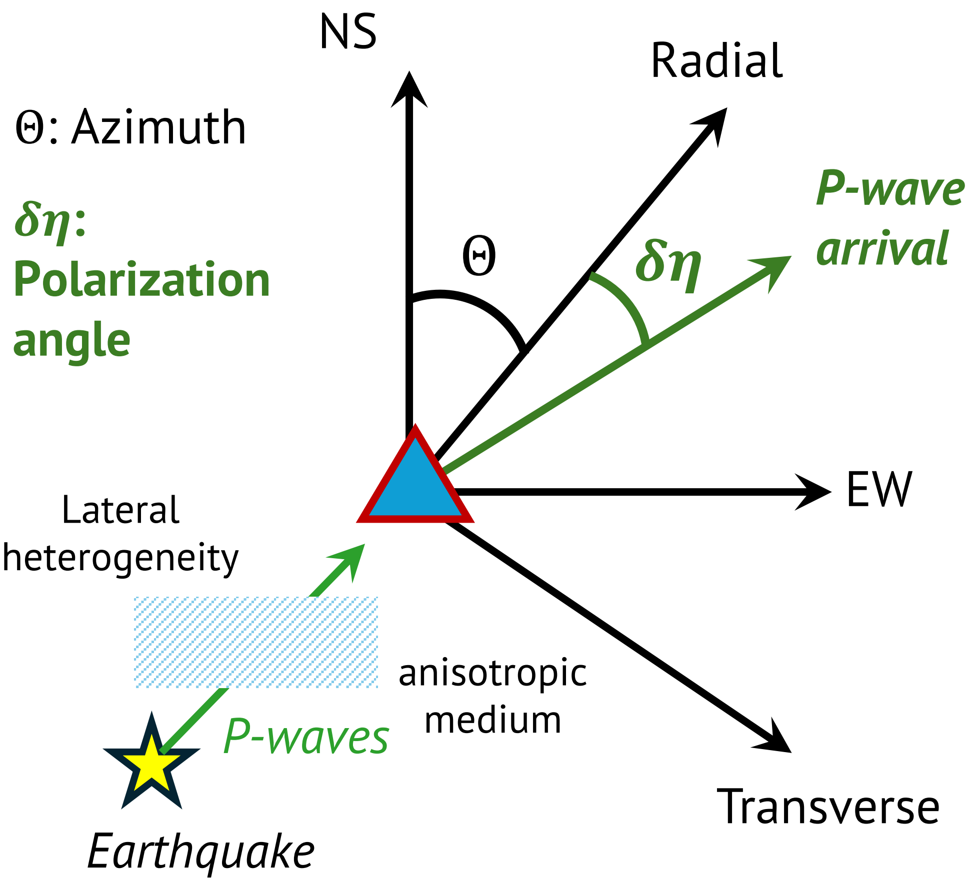

Figure S1: Schematic illustration of teleseismic P-wave polarization. In an isotropic and laterally homogeneous medium, teleseismic P waves are expected to oscillate in the vertical-radial plane. In contrast, in a laterally heterogeneous or anisotropic medium, P-wave particle motions and arrival angles can be deflected, resulting in polarization anomalies.

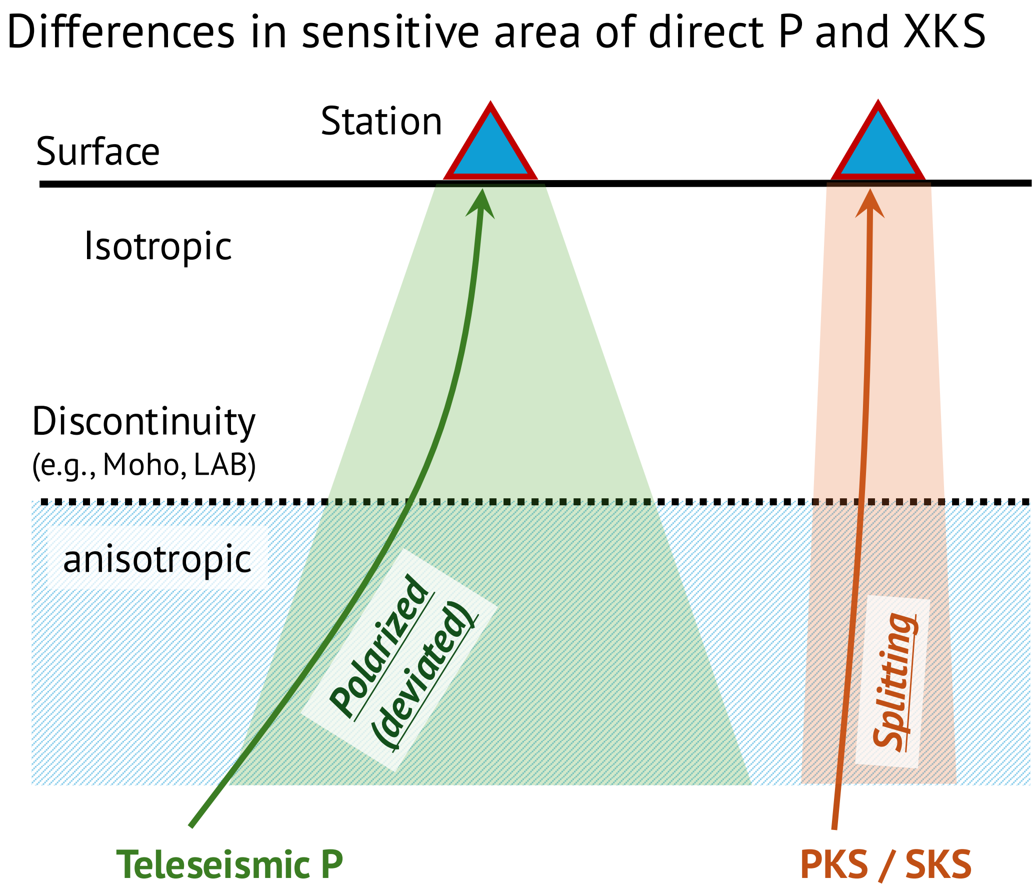

Figure S2: Schematic illustration of sampling geometry of teleseismic P-waves and PKS/SKS (XKS) phases. Teleseismic P-waves propagate along oblique ray paths and sample structure laterally offset from the station, whereas XKS phases with steep incident angles primarily sample structure directly beneath the receiver. This difference in sampling geometry leads to differences in the inferred anisotropic properties.

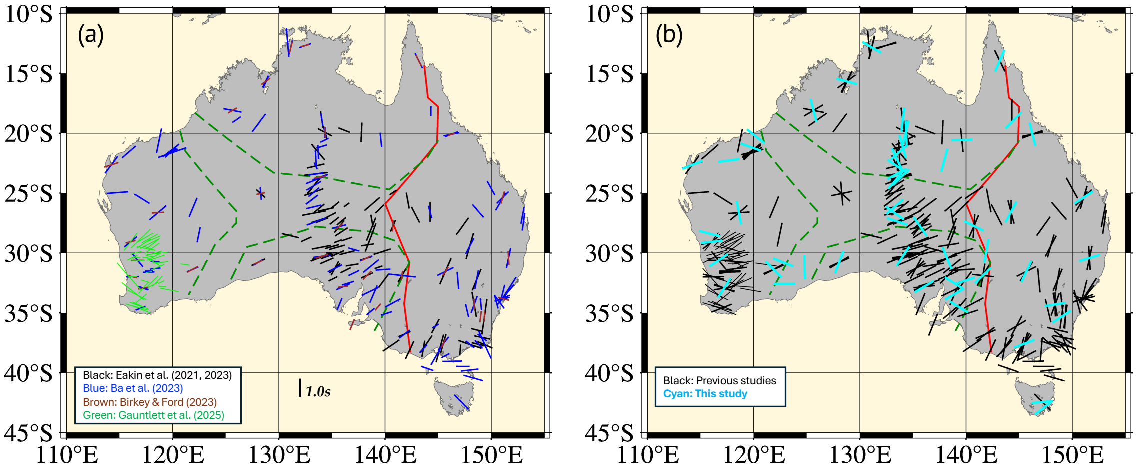

Figure S3: Comparison of fast-axis directions inferred from PKS/SKS (XKS) splitting analyses and from harmonic analysis of P-wave polarization anomalies. (a) Fast-axis directions from five recent XKS studies (Ba et al., 2023; Birkey and Ford, 2023; Eakin et al., 2023, 2021; Gauntlett et al., 2025). Colors indicate individual studies as shown in the legend. Red solid and green dashed lines show the Tasman Line and cratonic boundaries, respectively, as in Figure 1 (a). (b) Comparisons between the recent XKS-derived fast-axis directions and those inferred in this study. Black and cyan bars represent the previous XKS and the current P-wave polarization results, respectively. For clarity, the lengths of the bars are normalized by delay time for the XKS results and by the amplitude of the 2ϕ harmonic terms for our P-wave results.

Ba, K., Gao, S.S., Song, J., Liu, K.H., 2023. Seismic Azimuthal Anisotropy Beneath a Fast Moving Ancient Continent: Constraints From Shear Wave Splitting Analysis in Australia. J Geophys Res Solid Earth 128. https://doi.org/10.1029/2022jb025866

Birkey, A., Ford, H.A., 2023. Anisotropic structure of the Australian continent. Frontiers Earth Sci 10, 1055480. https://doi.org/10.3389/feart.2022.1055480

Eakin, C.M., Davies, D.R., Ghelichkhan, S., O'Donnell, J.P., Agrawal, S., 2023. The Influence of Lithospheric Thickness Variations Beneath Australia on Seismic Anisotropy and Mantle Flow. Geochem., Geophys., Geosystems 24. https://doi.org/10.1029/2023gc011066

Eakin, C.M., Flashman, C., Agrawal, S., 2021. Seismic anisotropy beneath Central Australia: A record of ancient lithospheric deformation. Tectonophysics 820, 229123. https://doi.org/10.1016/j.tecto.2021.229123

Gauntlett, M., Eakin, C.M., Bishoyi, N., Zhang, P., O'Donnell, J. -P., Murdie, R.E., Miller, M.S., Pickle, R., Ebrahimi, R., 2025. Seismic Anisotropy Analysis Across Southwestern Australia Reveals ENE-Trending Lithospheric Architecture Linked to Archean Yilgarn Craton Formation. Geochem., Geophys., Geosystems 26. https://doi.org/10.1029/2025gc012589